A High-order Discontinuous Galerkin Scheme for Elastic Wave Propagation

Nathalie Glinsky, Serge Moto Mpong, Sarah Delcourte

INRIA

INSTITUT NATIONAL DE RECHERCHE EN INFORMATIQUE ET EN AUTOMATIQUE

A High-order Discontinuous Galerkin Scheme for Elastic Wave Propagation

Nathalie Glinsky — Serge Moto Mpong — Sarah Delcourte

N° 7476

November 2010

Thème NUM

ISSN 0249-6399 ISRN INRIA/RR--7476--FR+ENG

INSTITUT NATIONAL
DE RECHERCHE
EN INFORMATIQUE
ET EN AUTOMATIQUE

INRIA

centre de recherche
SOPHIA ANTIPOLIS - MÉDITERRANÉE

A High-order Discontinuous Galerkin Scheme for Elastic Wave Propagation

Nathalie Glinsky*, Serge Moto Mpong†, Sarah Delcourte‡

Thème NUM — Systèmes numériques
Équipes-Projets Nachos

Rapport de recherche n° 7476 — November 2010 — 21 pages

Abstract: In this paper, we introduce a fourth-order leap-frog time scheme combined with a high-order discontinuous Galerkin method for the solution of the elastodynamic equations. The time discretization, obtained via a simple construction based on Taylor developments, provides an accurate scheme for the numerical simulation of seismic wave propagation. Results of the propagation of an eigenmode allow a numerical study of stability and convergence of the scheme for both uniform and non structured meshes proving the high level of accuracy of the method. The robustness of the scheme in the heterogeneous case is studied and we also examine the propagation of an explosive source in a homogeneous half-space.

Key-words: elastodynamic equation, velocity-stress formulation, discontinuous Galerkin method, high-order method, leap-frog scheme

* LCPC/CETE Nice and INRIA Sophia Antipolis Méditerranée, France
† University of Yahoundé, Cameroon
‡ University Claude Bernard Lyon 1, France

Centre de recherche INRIA Sophia Antipolis – Méditerranée
2004, route des Lucioles, BP 93, 06902 Sophia Antipolis Cedex
Téléphone : +33 4 92 38 77 77 — Télécopie : +33 4 92 38 77 65

Un schéma d'ordre élevé de type Galerkin discontinu pour la propagation d'ondes élastiques

Résumé : On présente un schéma saute-mouton en temps d'ordre quatre combiné à une méthode de type Galerkin discontinu d'ordre élevé en espace pour la résolution des équations de l'élastodynamique. La discrétisation temporelle, simplement déduite de développements de Taylor, permet d'obtenir un schéma précis pour la simulation numérique de la propagation d'ondes sismiques. Une étude numérique de la stabilité et de la convergence du schéma, via l'étude de la propagation d'un mode propre utilisant des maillages uniformes et non structurés, prouve la précision de la méthode. La robustesse du schéma est étudiée dans le cas d'un milieu hétérogène et l'on s'intéresse également à la propagation d'une source explosive dans un demi-espace homogène.

Mots-clés : équation élastodynamique, système vitesse-contrainte, méthode Galerkin discontinu, méthode d'ordre élevé, schéma saute-mouton

1 Introduction

Computational seismology has become a very important discipline for accurate estimates of ground motion thanks to constant increase of computational resources, a better understanding of physical phenomena and numerical solvers able to compute accurate solutions. Many different numerical methods have been developed within the last few decades. The most popular is the finite difference (FD) method [15] and its many extensions and improvements since the early staggered FD scheme (for instance [10] among many authors). Their major drawback is the restriction to rectangular grids not suited for geometrical internal or free surface irregularities. Other methods have been further developed such as finite element (FE) methods [12] which allow meshes adapted to complex geometries. However, they are more costly due to the inversion a global mass matrix at each time step. This difficulty was overcome by the use of Gauss-Lobato Legendre quadrature formulae and the spectral element methods (SEM) have been widely applied to quadrangular and hexaedral meshes (see [9] amongst many contributions). The use of triangular meshes permits a better aproximation of the medium (topography, faults). For this reason, we study a high-order Discontinuous Galerkin (DG) method applied to triangular meshes.

The Discontinuous Galerkin (DG) method has been initialy introduced by Reed and Hill [11] for the solution of neutron transport problems. Neglected during twenty years, it became very popular to solve hyperbolic problems especially in computational electromagnetics [5]. In spite of its succes in many domains of applications, this method has been rarely applied to seismic wave propagation problems. Käser et al. (see [8] and references herein) proposed a DG finite element scheme that uses the ADER approach based on an upwind scheme in order to solve the elastic wave equations with the same high accuracy in both space and time.

We study the P-SV wave propagation considering an isotropic, linearly elastic medium by solving the velocity-stress formulation of the elastodynamic equations. For the discretization of this system, we focus on a DG method which is a finite element method allowing discontinuities at the interfaces treated by numerical fluxes as for finite volumes [1]. Our method is based on a numerical flux function depending on averaged field values and a leap-frog time-discretization which leads to a non-dissipative scheme. The discrete energy of the system is preserved by the method in infinite domains [3]. The method is suitable for complex unstructured triangular meshes. The extension to higher order in space is realized by Lagrange polynomial functions (of degree 0 to 4 for our solver), defined locally on triangles and do not necessitate the inversion of a global mass matrix since an explicit scheme in time is used. According to the first results of the method presented in [3], the time accuracy of the scheme is crucial when global high-order accuracy is required. Then, we propose an extension of the leap-frog scheme to higher orders of accuracy following a method proposed for the Maxwell equations by Young [16] or Spachmann et al. [14] and applied to DG methods by Fahs [4]. This method allows us to achieve temporal accuracy to any even order desired by introducing an iterative procedure. We restrict here ourselves to the fourth-order leap-frog scheme since we consider fourth degree polynomial functions at the most.

This article is organized as follows. In section 2, we present the equation system and the spatial discretization by a DG method. Then, in section 3, we

detail the leapfrog scheme and its higher-order extension. Finally, sections 4, 5 and 6 present numerical results. First, we propose a stability and convergence study of the scheme applied to the eigenmode propagation problem. Secondly, we examine the propagation of a pulse in a heterogeneous medium. Finally, we study the propagation of an explosive source in a homogeneous half-space.

2 Equations and spatial discretization

In a linear, isotropic and infinite medium, the P-SV wave propagation is modelled by the elastodynamic equation

$$\rho \partial_{tt} \vec{u} = \nabla \cdot \underline{\sigma},$$

where $\vec{u}$ is the displacement vector, $\underline{\sigma}$ the stress tensor and ρ the density of the medium. Relating the stress tensor to the displacement vector components and introducing the velocity vector $\vec{v} = \partial_t \vec{u}$, we choose to solve the first-order velocity-stress formulation (as in [15]) which writes

$$\left\{ \begin{array}{rcl} \rho \partial_t \vec{v} & = & \nabla \cdot \underline{\sigma}, \\ \partial_t \underline{\sigma} & = & \lambda (\nabla \cdot \vec{v}) \underline{I} + \mu (\nabla \vec{v} + (\nabla \vec{v})^t), \end{array} \right. \tag{1}$$

where $\underline{I}$ is the identity matrix and λ and μ are the Lamé coefficients describing the rheology of the medium, related to the P- and S-waves velocities by

$$V_P = \sqrt{\frac{\lambda + 2\,\mu}{\rho}} \quad \text{and} \quad V_S = \sqrt{\frac{\mu}{\rho}}\,.$$

System (1) is closed by adding physical boundary conditions at the free surface of the medium : $\underline{\sigma}\,\vec{n} = \vec{0}$, where $\vec{n}$ is the vector normal to the free surface. External forces are neglected.

Since the stress tensor is symmetrical, we replace it by a vector containing three independent components. Then, the unknown vector $\vec{W}$ writes $\vec{W} = (v_x, v_y, \sigma_{xx}, \sigma_{yy}, \sigma_{xy})^t$ and (1) expresses in matrix form

$$\partial_t \vec{W} - \sum_{\alpha \in \{x,y\}} \underline{A}_\alpha(\rho, \lambda, \mu)\, \partial_\alpha \vec{W} = 0\,. \tag{2}$$

For the spatial discretization of this system, we approximate the physical domain by a polygon Ω, discretized in N_T triangles T_i forming a partition of the domain. Each equation of (2) is multiplied by a scalar test function $\phi_k^{T_i}$ and integrated on each element T_i. The characteristics of the medium (ρ, λ, μ) are assumed to be constant over each element T_i; to simplify the notations, we denote by $\underline{A}_\alpha^{T_i}$, in what follows, the restriction of the matrix $\underline{A}_\alpha(\rho, \lambda, \mu)$ to T_i. Applying the Green's identity, we obtain

$$\int_{T_i} \partial_t \vec{W}\, \phi_k^{T_i}\, dx\, dy + \sum_{\alpha \in \{x,y\}} \underline{A}_\alpha^{T_i} \int_{T_i} \vec{W} \partial_\alpha \phi_k^{T_i}\, dx\, dy - \underline{A}_n^{T_i} \int_{\partial T_i} \vec{W}\, \phi_k^{T_i}\, ds = 0\,, \tag{3}$$

where $\vec{n}$ is the outward unit normal vector to T_i and

$$\underline{A}_n^{T_i} = \sum_{\alpha \in \{x,y\}} n_\alpha\, \underline{A}_\alpha\,(\rho, \lambda, \mu)\,.$$

As test functions, we choose the standard Lagrange nodal interpolants $\phi_k^{T_i} \in \mathcal{P}_m(T_i)$, set of polynomials of degree m locally defined on the element T_i. Their expression can be found in [2]. For a fixed degree m and a space dimension d, the number of basis functions of T_i is $N_m = (m+1)...(m+d)/d!$. Each component W of the vector $\vec{W}$ is approximated on T_i by

$$W_{|T_i}(x,y,t) = \sum_{j=1}^{N_m} W_j^{T_i}(t)\ \phi_j^{T_i}(x,y)\ ,$$

where N_m is also the number of degrees of freedom on T_i. The unknowns of the problem are N_m values in each element T_i for each of the 5 components of $\vec{W}$. Thus, the total number of unknowns is $N_m \times 5 \times N_T$. Including this approximation in (3), the first term writes

$$\forall k = 1,..,N_m\ ,$$
$$\int_{T_i} \partial_t \vec{W}\, \phi_k^{T_i}\, dx\, dy = \sum_{j=1}^{N_m} \underline{M}_{kj}^{T_i} \frac{d}{dt} \vec{W}_j^{T_i} \quad \text{and} \quad \underline{M}_{kj}^{T_i} = \int_{T_i} \phi_j^{T_i}\, \phi_k^{T_i}\, dx\, dy\,,$$

where $\underline{M}^{T_i}$ is the mass matrix in the element T_i. Following the same method for the second integral of (3), we obtain

$$\forall k = 1,..,N_m\ ,$$
$$\sum_{\alpha\in\{x,y\}} \underline{A}_\alpha^{T_i} \int_{T_i} \vec{W}\, \partial_\alpha \phi_k^{T_i}\, dx\, dy = \sum_{\alpha\in\{x,y\}} \underline{A}_\alpha^{T_i} \sum_{j=1}^{N_m} \underline{G}_{\alpha,kj}^{T_i}\, \vec{W}_j^{T_i}$$

where

$$\underline{G}_{\alpha,kj}^{T_i} = \int_{T_i} \phi_j^{T_i}\, \partial_\alpha \phi_k^{T_i}\, dx\, dy\,.$$

For the last term of (3), the integral on ∂T_i, we first split this boundary in internal and boundary faces. We define $N(i)$ the set of the indices of the neighboring elements of T_i and F_{il} denotes each internal face common to the elements T_i and T_l i.e. $F_{il} = T_i \cap T_l$. Finally, $B(i)$ is the set of the indices l of the faces which are common to T_i and the boundary of the domain $\partial\Omega$. Such faces are denoted by $F_l^{B_i} = T_i \cap \partial\Omega$ for $l \in B(i)$ and for most elements, the set $B(i)$ is empty. The splitting of the boundary leads to

$$\underline{A}_n^{T_i} \int_{\partial T_i} \vec{W}\, \phi_k^{T_i}\, ds = \sum_{l\in N(i)} \underline{A}_n^{T_i} \int_{F_{il}} \vec{W}\, \phi_k^{T_i}\, ds + \sum_{l\in B(i)} \underline{A}_n^{T_i} \int_{F_l^{B_i}} \vec{W}\, \phi_k^{T_i}\, ds\,. \quad (4)$$

For an interior face, the associated boundary integral term is computed via the average value on this face $\vec{W}_{|F_{il}} = \left(\vec{W}^{T_i} + \vec{W}^{T_l}\right)/2$, then, the first integral of (4) becomes

$$\forall k = 1,..,N_m\ ,$$
$$\underline{A}_n^{T_i} \sum_{l\in N(i)} \int_{F_{il}} \vec{W}\, \phi_k^{T_i}\, ds = \frac{1}{2} \underline{A}_n^{T_i} \sum_{l\in N(i)} \sum_{j=1}^{N_m} \left[\left(\underline{R}_{|F_{il}}^{T_i}\right)_{kj} \vec{W}_j^{T_i} + \left(\underline{R}_{|F_{il}}^{T_l}\right)_{kj} \vec{W}_j^{T_l} \right]\ , \quad (5)$$

where the matrices write respectively

$$\left(\underline{R}^{T_i}_{|F_{il}}\right)_{kj} = \int_{F_{il}} \phi_j^{T_i}\phi_k^{T_i}\,ds \quad \text{and} \quad \left(\underline{R}^{T_l}_{|F_{il}}\right)_{kj} = \int_{F_{il}} \phi_j^{T_l}\phi_k^{T_i}\,ds\,. \tag{6}$$

For a face $F_l^{B_i}$ on the boundary of the domain, the free surface condition $\underline{\sigma}\,\vec{n} = \vec{0}$ is introduced weakly in the second term of (4). This condition only affects the stress components, the velocity in the face being considered equal to its value in T_i. Then, the second integral of (4) reduces to

$$\begin{aligned} &\forall k = 1,..,N_m\,,\\ &\underline{A}_n^{T_i}\sum_{l\in B(i)}\int_{F_l^{B_i}} \vec{W}\phi_k^{T_i}\,ds = \underline{A}_n^{T_i}\sum_{l\in B(i)}\sum_{j=1}^{N_m}\left(\underline{R}^{T_i}_{|F_l^{B_i}}\right)_{kj}\left(\vec{W}^{T_i}_{|F_l^{B_i}}\right)_j \end{aligned} \tag{7}$$

where, at the boundary face $\vec{W}_{|F_l^{B_i}} = \left(v_x^{T_i}, v_y^{T_i}, 0, 0, 0\right)^t$ and $\left(\underline{R}^{T_i}_{|F_l^{B_i}}\right)_{kj}$ is calculated as in (6). Finally, we define the vectors $\vec{V}_\alpha^{T_i}$ ($\alpha = x, y$) and $\vec{S}_{\alpha\beta}^{T_i}$ ($\alpha, \beta = x, y$) which contain respectively the N_m values of the velocity component v_α and the three stress component $\sigma_{\alpha\beta}$ in the element T_i. Thus, the spatial discretisation is summarized by

$$\left\{\begin{array}{lll} \underline{M}^{T_i}\dfrac{d}{dt}\vec{V}_\alpha^{T_i} & = F_\alpha^{T_i}\left(\vec{S}\right) & \alpha = x, y\,,\\ \underline{M}^{T_i}\dfrac{d}{dt}\vec{S}_{\alpha\beta}^{T_i} & = G_{\alpha\beta}^{T_i}\left(\vec{V}\right) & \alpha, \beta = x, y\,, \end{array}\right. \tag{8}$$

where F_α and $G_{\alpha\beta}$ are discrete operators collecting the integrals on T_i and ∂T_i. Note that F_α (respectively $G_{\alpha\beta}$) depends only on the stress components $\vec{S}$ (respectively the velocity components $\vec{V}$) and that the subscript and the superscript have been deliberately omitted since all the velocities components (respectively the stress components) are involved and the integrals on ∂T_i also need values in the neighboring elements of T_i.

3 Time discretization

For the time discretization, we apply an explicit leap-frog scheme ([5], [1], [3]) which results, when combined with the flux (5), in a non-dissipative scheme [3]

$$\left\{\begin{array}{lll} \underline{M}^{T_i}\dfrac{\left(\vec{V}_\alpha^{T_i}\right)^{n+1} - \left(\vec{V}_\alpha^{T_i}\right)^{n}}{\Delta t} & = F_\alpha^{T_i}\left(\vec{S}^{n+\frac{1}{2}}\right) & \alpha = x, y\,,\\ \underline{M}^{T_i}\dfrac{\left(\vec{S}_{\alpha\beta}^{T_i}\right)^{n+\frac{3}{2}} - \left(\vec{S}_{\alpha\beta}^{T_i}\right)^{n+\frac{1}{2}}}{\Delta t} & = G_{\alpha\beta}^{T_i}\left(\vec{V}^{n+1}\right) & \alpha, \beta = x, y\,, \end{array}\right. \tag{9}$$

where Δt is the time step of the scheme. Note that the initialisation of the scheme needs the velocities at $t = t_0$ and the stresses at $t = t_0 + \frac{\Delta t}{2}$. This time discretization scheme is easy to implement and has nice mathematical properties; it is especially well adapted to the matrices $\underline{A}_\alpha$ which are extradiagonal by blocks. But, since it is second order accurate, the global accuracy of the scheme

can be penalized by the time approximation when higher-degree polynomials ($m > 2$) are used for spatial approximation. Then, we propose a higher-order leap-frog scheme following the method, proposed for the Maxwell equations, by Young [16] or Spachmann et al. [14] and applied to a discontinuous Galerkin method by Fahs [4]. For a detailed description of the method, we introduce a simplified two equations problem whose unknowns are $v(x,t)$ and $\sigma(x,t)$

$$\partial_t v = f(\sigma) \quad \text{and} \quad \partial_t \sigma = g(v) \,. \tag{10}$$

From Taylor developments, we can derive a leap-frog scheme based on velocities at even time steps and stresses at odd time steps. We rather choose to divide the time step by two and we obtain, for simplified system (10)

$$\left\{ \begin{array}{rclcl} v^{n+1} & = & v^n & + & \Delta t \partial_t v^{n+\frac{1}{2}} + \dfrac{\Delta t^3}{24} \partial_{ttt} v^{n+\frac{1}{2}} + O(\Delta t^5) \,, \\ \sigma^{n+\frac{3}{2}} & = & \sigma^{n+\frac{1}{2}} & + & \Delta t \partial_t \sigma^{n+1} + \dfrac{\Delta t^3}{24} \partial_{ttt} \sigma^{n+1} + O(\Delta t^5) \,. \end{array} \right. \tag{11}$$

Firstly, the evaluation of $\partial_t v^{n+\frac{1}{2}}$ and $\partial_t \sigma^{n+1}$ is done thanks to (10) at times $\left(n+\frac{1}{2}\right)\Delta t$ for v and $(n+1)\,\Delta t$ for σ. Considering only these derivatives in (11) and neglecting the higher-order terms leads to the classical second-order leap-frog scheme

$$\left\{ \begin{array}{rclcl} v^{n+1} & = & v^n & + & \Delta t\, f\left(\sigma^{n+\frac{1}{2}}\right) \\ \sigma^{n+\frac{3}{2}} & = & \sigma^{n+\frac{1}{2}} & + & \Delta t\, g\left(v^{n+1}\right) , \end{array} \right.$$

which also writes in the following form

$$\left\{ \begin{array}{rclcl} v^{n+1} & = & v^n & + & \Delta t\, v_\star^{n+\frac{1}{2}} \\ \sigma^{n+\frac{3}{2}} & = & \sigma^{n+\frac{1}{2}} & + & \Delta t\, \sigma_\star^{n+1} , \end{array} \right.$$

with $v_\star^{n+\frac{1}{2}} = f(\sigma^{n+\frac{1}{2}})$ and $\sigma_\star^{n+1} = g(v^{n+1})$. When applied to the discrete system (8), it is equivalent to the standard leap-frog scheme (9).

The construction of an higher-order leap-frog scheme needs values for $\partial_{ttt} v^{n+\frac{1}{2}}$ and $\partial_{ttt} \sigma^{n+1}$, which are obtained, as previously, by successive derivatives of (10). We then obtain a fourth-order leap-frog scheme

$$\left\{ \begin{array}{rclcl} v^{n+1} & = & v^n & + & \Delta t\, v_\star^{n+\frac{1}{2}} + \dfrac{\Delta t^3}{24}\, v_{\star\star}^{n+\frac{1}{2}} \\ \sigma^{n+\frac{3}{2}} & = & \sigma^{n+\frac{1}{2}} & + & \Delta t\, \sigma_\star^{n+1} + \dfrac{\Delta t^3}{24}\, \sigma_{\star\star}^{n+1} , \end{array} \right. \tag{12}$$

$$\text{with} \quad \left\{ \begin{array}{l} v_\star^{n+\frac{1}{2}} = f\left(\sigma^{n+\frac{1}{2}}\right) , \\ \sigma_\bullet^{n+\frac{1}{2}} = g\left(v_\star^{n+\frac{1}{2}}\right) , \\ v_{\star\star}^{n+\frac{1}{2}} = f\left(\sigma_\bullet^{n+\frac{1}{2}}\right) , \end{array} \right. \quad \text{and} \quad \left\{ \begin{array}{l} \sigma_\star^{n+1} = g\left(v^{n+1}\right) , \\ v_\bullet^{n+1} = f\left(\sigma_\star^{n+1}\right) , \\ \sigma_{\star\star}^{n+1} = g\left(v_\bullet^{n+1}\right) . \end{array} \right.$$

This method is applied to (2) using the spatial discretization (8) and a fourth-order leap-frog scheme writes

$$\left\{\begin{array}{ll}\left(\vec{V}_\alpha^{T_i}\right)^{n+1} & = \left(\vec{V}_\alpha^{T_i}\right)^{n} + \Delta t \left(\vec{V}_\alpha^{T_i}\right)_\star^{n+\frac{1}{2}} + \dfrac{\Delta t^3}{24}\left(\vec{V}_\alpha^{T_i}\right)_{\star\star}^{n+\frac{1}{2}} \qquad \alpha = x, y\,, \\ \left(\vec{S}_{\alpha\beta}^{T_i}\right)^{n+\frac{3}{2}} & = \left(\vec{S}_{\alpha\beta}^{T_i}\right)^{n+\frac{1}{2}} + \Delta t \left(\vec{S}_{\alpha\beta}^{T_i}\right)_\star^{n+1} + \dfrac{\Delta t^3}{24}\left(\vec{S}_{\alpha\beta}^{T_i}\right)_{\star\star}^{n+1} \qquad \alpha, \beta = x, y\,,\end{array}\right. \tag{13}$$

with

$$\left\{\begin{array}{ll}\left(\vec{V}_\alpha^{T_i}\right)_\star^{n+\frac{1}{2}} & = \left(\underline{M}^{T_i}\right)^{-1} F_\alpha^{T_i}\left(\vec{S}^{n+\frac{1}{2}}\right)\,, \\ \left(\vec{S}_{\alpha\beta}^{T_i}\right)_\bullet^{n+\frac{1}{2}} & = \left(\underline{M}^{T_i}\right)^{-1} G_{\alpha,\beta}^{T_i}\left(\vec{V}_\star^{n+\frac{1}{2}}\right)\,, \\ \left(\vec{V}_\alpha^{T_i}\right)_{\star\star}^{n+\frac{1}{2}} & = \left(\underline{M}^{T_i}\right)^{-1} F_\alpha^{T_i}\left(\vec{S}_\bullet^{n+\frac{1}{2}}\right)\,,\end{array}\right.$$

and

$$\left\{\begin{array}{ll}\left(\vec{S}_{\alpha\beta}^{T_i}\right)_\star^{n+1} & = \left(\underline{M}^{T_i}\right)^{-1} G_{\alpha,\beta}^{T_i}\left(\vec{V}^{n+1}\right)\,, \\ \left(\vec{V}_\alpha^{T_i}\right)_\bullet^{n+1} & = \left(\underline{M}^{T_i}\right)^{-1} F_\alpha^{T_i}\left(\vec{S}_\star^{n+1}\right)\,, \\ \left(\vec{S}_{\alpha\beta}^{T_i}\right)_{\star\star}^{n+1} & = \left(\underline{M}^{T_i}\right)^{-1} G_{\alpha,\beta}^{T_i}\left(\vec{V}_\bullet^{n+1}\right)\,.\end{array}\right.$$

In practice, for a given approximation in space, the fourth-order leap-frog scheme needs three times more arithmetic operations (to calculate the fluxes F and G when the classical leap-frog scheme necessitates only one) and two times more memory storage since additional arrays have to be defined for $\left(\vec{V}_\alpha^{T_i}\right)_{\star\star}^{n+\frac{1}{2}}$ and $\left(\vec{S}_{\alpha\beta}^{T_i}\right)_{\star\star}^{n+1}$. Following the same procedure, higher-order (sixth, eighth and more) leap-frog schemes could be derived.

4 Stability and convergence study

We realize some numerical studies of the properties of the method. A mathematical analysis of the stability and convergence of this new scheme is underway and will be the subject of a further publication.

The method has been first applied to the propagation of an eigenmode. The computational domain $\mathcal{D}$ is the unit square and free surface boundary conditions are applied on all boundaries. We consider the (1,1) mode whose exact solution is

$$\left\{\begin{array}{rrl} v_x = & a & (\cos\pi x)\,(\sin\pi y)\,(\cos at) \\ v_y = & -a & (\sin\pi x)\,(\cos\pi y)\,(\cos at) \\ \sigma_{xx} = & -b & (\sin\pi x)\,(\sin\pi y)\,(\sin at) \\ \sigma_{yy} = & b & (\sin\pi x)\,(\sin\pi y)\,(\sin at) \\ \sigma_{xy} = & 0 & \end{array}\right. \tag{14}$$

where $a = \sqrt{2}\pi V_s$ and $b = 2\pi\mu$. The medium properties are $\rho = 1$, $\lambda = 0.5$ and $\mu = 0.25$ leading to P and S waves velocities respectively equal to $V_p = 1$ and $V_S = 0.5$. The initialisation of the leap-frog scheme is done from the exact solution (14) at $t = 0$ for v and $t = \frac{\Delta t}{2}$ for σ, Δt being the time step of the scheme. In what follows, the notation Pk-LFi (k=1,..., 4 and i=2 or 4) refers

to a spatial discretization based on polynomial basis of degree k and a classical second-order leap-frog time scheme (LF2) or its extension (LF4).

First, in order to check numerically the stability of the different methods, we solve this problem for different values of the time step. This time step depends on geometrical properties of the mesh and is proportional to a CFL value which is a data of the simulation. An optimal formula for the time step would provide a stable scheme until the value CFL=1 in the finite volume (P0) case but it is not easy to establish such a formula for unstructured meshes. Then, we simply set that

$$\Delta t = \min_{T_i} \frac{CFL \times h_i}{(V_p)_i} \,,$$

a formula deduced from the optimal stability condition for finite volumes applied to the reference triangle (as in [3]) and where the mesh spacing h_i is the smallest edge of the triangle T_i. We have performed such studies for all Pk-LFi combinations and the maximum values of the CFL numbers ensuring stability are given in the table 1. We conclude, from these results, that the value of the CFL number depends on both time and space schemes. Its value decreases when the spatial discretization order increases and the allowed time steps of the LF4 schemes are greater than those of the LF2 schemes. For any space scheme, we have

$$CFL_{LF4} \simeq 2.5 \times CFL_{LF2} \,.$$

Time/space discretization	P2	P3	P4
LF2	0.2322	0.1498	0.0939
LF4	0.5928	0.3821	0.2644

Table 1: Maximum value of the CFL number for different time and space discretization methods

For the convergence study of these schemes, the problem is solved using a series of meshes of different mesh spacing h. Uniform triangular meshes are obtained by splitting quadrangular cells in two triangles and unstructured meshes are constructed via a commercial mesher (Simail) from an uniform distribution of the nodes on the boundaries of the domain. The mesh spacing h is then the smallest edge in the mesh. All results correspond to solutions at time $t = 5.0$ s. We display, in figure 1, the L^2-error between computed and exact solutions in logarithmic scale as a function of h for different schemes applied to uniform (left figure) and unstructured meshes (right figure) and using the classical leap-frog scheme (LF2, first line of figures). The results prove a second order convergence for both types of meshes, even if the error level is lower for the highest order schemes. The use of higher degree basis functions do not improve the convergence of the scheme since the leap-frog scheme LF2 is second order accurate. We notice that results obtained using unstructured meshes are slightly better than those of uniform meshes. It is probably due to the choice of Delaunay meshes which have well known properties compared to the uniform meshes [3].

We present, in figure 1, the same results for the fourth-order leap-frog extension (LF4, second line of figures), for uniform (left figure) and unstructured meshes (right figure). The improvement of the convergence is obvious when using the high-order time scheme for both types of meshes, in particular for P3-LF4 and P4-LF4 methods, a fourth-order convergence being obtained with

the last scheme. This proves that the use of fourth-degree basis functions (P4) is optimal when combined to a fourth-order time scheme (LF4). In summary, the values of the convergence orders of the different methods, are gathered in the table 2 and confirm the results of the figures.

Finally, we examine the efficiency of the different methods by plotting, for uniform meshes, the evolution of the L^2-error at time $t = 5.0$ s as a function of the CPU time of the simulation. We note, in figure 2, that for a given level of accuracy, 10^{-4} for instance, the two most accurate methods (P3-LF4 and P4-LF4) are also the most efficient since the given error level is obtained for lower CPU times compared to other methods [7]. The ratio between the minimum and the maximum CPU times to reach the given level of accuracy, corresponding respectively to the P4-LF4 and P2-LF2 schemes is about 100. Despite the fact that the LF4 scheme needs more operations, higher-order schemes are more efficient as coarser meshes can be used to reach a desired accuracy level. Moreover, the use of greater times steps in the LF4 scheme case compensates for the overcost due to the multi-step procedure.

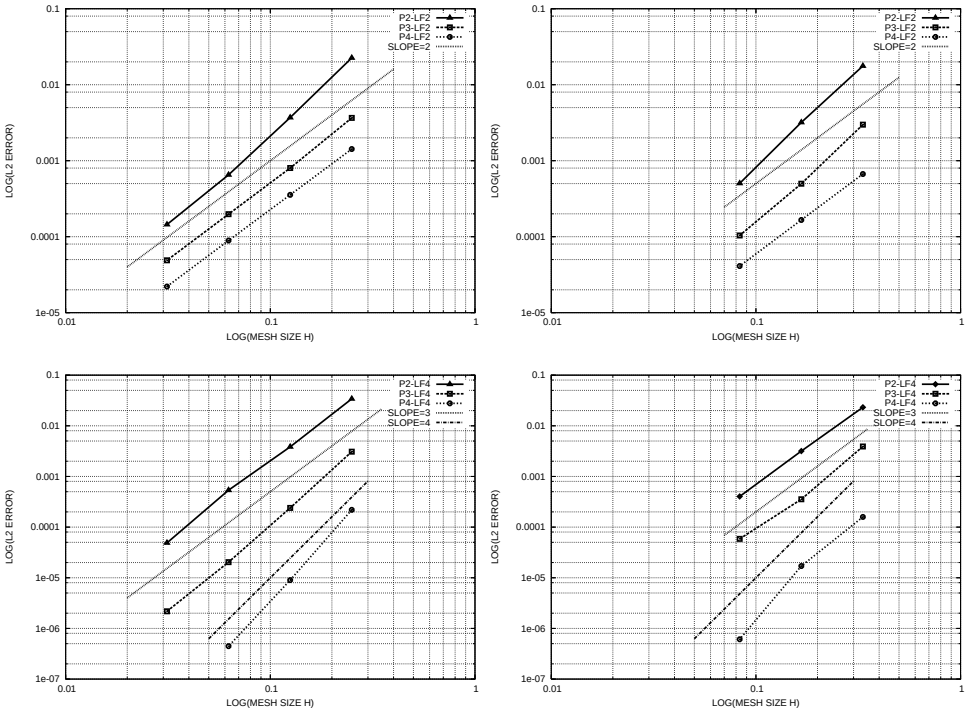

Figure 1: Convergence study. L^2-error as a function of the mesh spacing h for different Pk-LF2 schemes (k=2,3,4) (first line) and Pk-LF4 schemes (second line) using uniform (left) and unstructured meshes (right).

	Mesh	LF2	LF4		Mesh	LF2	LF4		Mesh	LF2	LF4
P2	Unif.	2.44	3.04	P3	Unif.	2.07	3.50	P4	Unif.	2.00	4.47
	Unstr.	2.57	2.92		Unstr.	2.42	3.03		Unst.	2.01	4.01

Table 2: Values of convergence orders for different methods Pk-LFi (k=2,3,4 and i=2 or 4) and the two types of meshes

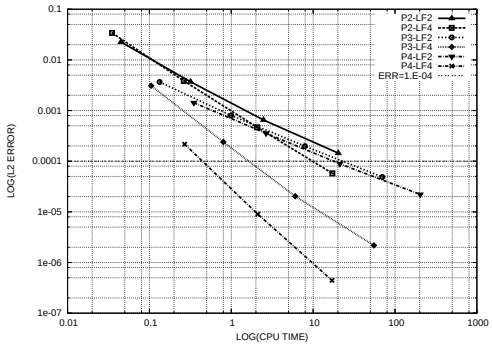

Figure 2: Efficiency of the methods. L^2-error at time $t = 5.0$ s as a function of CPU time for different schemes Pk-LFi (k=2,3,4, i=2 or 4), uniform meshes.

5 Propagation of a pulse

The second studied problem is the propagation of a pulse in a homogeneous or heterogeneous medium. This problem has already been examined in the homogeneous case by Delcourte et al. [3], especially the convergence study which, thus, is not tackled here. Our objective is to focus on the robustness of the scheme in the heterogeneous case. So,we restrict ourselves to the P2-LF2 scheme. The initial condition is given by :

$$\left\{ \begin{array}{ll} v_x(x,y,t=0) & = \exp^{-50(x-1)^2} \\ \sigma_{xx}(x,y,t=0) & = -\exp^{-50(x-1)^2}, \end{array} \right. \tag{15}$$

v_y, σ_{yy} and σ_{xy} being set to zero. The solution does not depend on y. The analytical solution in 1D is calculated using the characteristic method according to the initial condition at $t = 0$. For a homogeneous medium, it writes [3]

$$\begin{aligned} v_x(x,y,t) = \frac{1}{2}\Big[& v_x(x^-,t,y,0) + v_x(x^+,t,y,0) + \\ & \frac{1}{\rho\, V_P}\left(\sigma_{xx}(x^+,y,0) - \sigma_{xx}(x^-,y,0)\right)\Big] \\ \sigma_{xx}(x,y,t) = \frac{1}{2}\big[& \sigma_{xx}(x^-,y,0) + \sigma_{xx}(x^+,y,0) + \\ & \rho\, V_P\left(v_x(x^+,y,0) - v_x(x^-,y,0)\right)\big] \end{aligned} \tag{16}$$

where $x^+ = x + V_P\, t$ and $x^- = x - V_P\, t$. For clarity purpose, we do not detail the solution in the heterogeneous case. Three different media have been considered; their characteristics are listed in the table 3.

Medium 1	ρ_1= 1.0	$V_{P\,1}$=1.0	$V_{S\,1}$=0.5
Medium 2	ρ_2=1.0	$V_{P\,2}$=2.0	$V_{S\,2}$=1.0
Medium 3	ρ_3=1.0	$V_{P\,3}$=10.0	$V_{S\,2}$=5.0

Table 3: Density, P- and S- wave velocities for the three media of the pulse propagation test case

First, we consider the rectangular domain $[0.,4.]\times[0.,1.]$ containing the medium 1. The domain is discretized by a uniform mesh with $h=10^{-2}$m. On the boundaries of the domain, which correspond to a truncation of an infinite domain, we apply an absorbing upwind scheme (detailed in [3]) deduced from (5). For an absorbing edge B_i of T_i, we only consider the outgoing waves and neglect the contribution from outside. Then, this condition expresses

$$\forall k=1,..,N_m\,,\quad \underline{A}_n^{T_i}\int_{B_i}\vec{W}\,\phi_k^{T_i}\,ds=\left[\underline{A}_n^{T_i}\right]^+\sum_{j=1}^{N_m}\left(\underline{R}_{|B_i}^{T_i}\right)_{kj}\vec{W}_j^{T_i}$$

where $\underline{A}_n=\underline{A}_n^+ + \underline{A}_n^-$ with $\underline{A}_n^+=\underline{P}\,\underline{L}^+\,\underline{P}^{-1}$ where $\underline{L}^+$ contains only positive eigenvalues. As previously, the matrix R is given by (6). The initial condition for the leap-frog scheme is deduced from (15) at staggered times, as previously for the eigenmode problem. We analyze the solution for v_x on the line $y=0.5$. The error in L^2 norm at time $n\,\Delta t$ between exact (16) and computed solutions is

$$err_{L^2}^n=\left\{\sum_{i=1}^{N}h\left[(v_x(x_i,0.5,n\,\Delta t)-(v_x)_i^n)^2+\left(\sigma_{xx}(x_i,0.5,(n+1/2)\Delta t)-(\sigma_{xx})_i^{n+1/2}\right)^2\right]\right\}^{1/2}$$

where N is the number of points on the line $y=0.5$.

We present, in figure 3, the computed velocity v_x at times t_1 =0.25s, t_2 =1.0s and t_3 =2.0s and the error between exact and computed solutions multiplied by a factor 10 :

$$ERR(x_i)=10.\times(v_x(x_i,0.5,t)-(v_x)_i^n)\ .$$

On the first figure, at time t_1, we notice a low level of error which propagates in both directions as visible on the two next figures. At time t_2, the part of the error moving backward has reached the left boundary of the domain and is out at time t_3.

We now consider the domain $[0.,6.]\times[0.,1.]$ containing the medium 1 for $x\le 2.0$ and the medium 2 elsewhere. The ratio between velocities of both media is $V_{P\,2}/V_{P\,1}$=2 and the time step in the entire domain is calculated from the highest velocity, that is $V_{P\,2}$. So, the time step $\Delta t_2=0.5\times\Delta t_1$.

We plot, in figure 4, the velocity v_x and the error at times t_1, t_2 and t_3. The result obtained at t_1, on the first figure, is comparable to the homogeneous case but with a lower error level. This is probably due to the use of a smaller time step Δt_2 in the medium 1. At time t_2, le pulse crosses the interface between both media. The scheme remains stable and no spurious reflection has been generated by the scheme. At time t_3, the incident pulse is completely in the medium 2 and the reflected part can be observed in the medium 1.

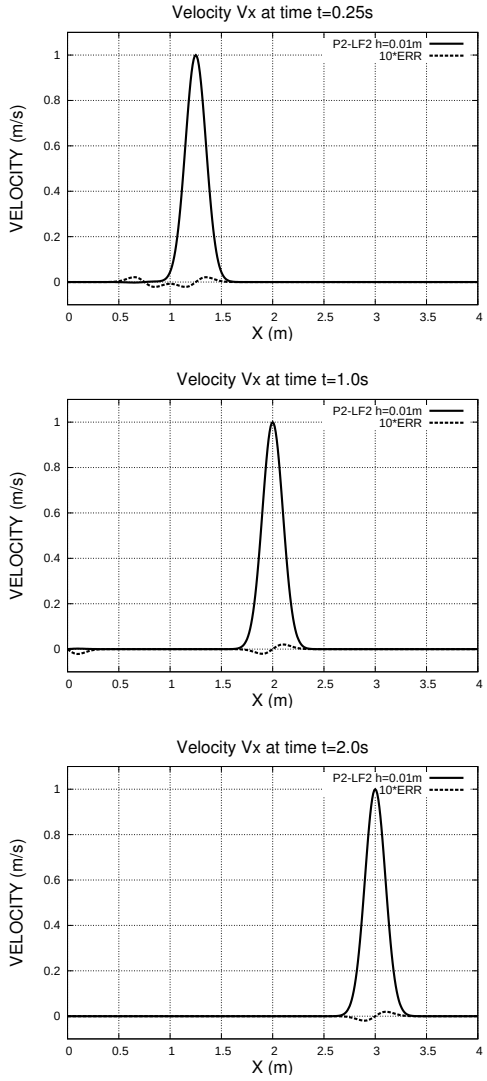

Figure 3: Propagation of a pulse in a homogeneous medium. Velocity v_x and error on the line $y = 0.5$ at times t_1=0.25s, t_2=1.0s and t_3=2.0s.

Finally, we consider the domain $[0., 16.] \times [0., 1.]$ containing the medium 1 for $x \leq 2.0$ and the medium 3 in the right part. Now, the ratio between velocities of both media is $V_{P\,3}/V_{P\,1}$=10 leading to a time step $\Delta t_3 = 0.1 \times \Delta t_1$. As before, we plot, on figure 5, the velocity v_x and the error at t_1, t_2 and t_3. The results are comparable to the previous heterogeneous case. This proves the robustness of the approximation scheme, even when the ratio between velocities of both media is equal to 10.

We present in table 4, the errors in L^2 and L^∞ norms at differents times. During the propagation of the pulse, the error level in L^∞ norm remains constant and a decrease of the value in L^2 norm occurs when the error wave reaches the

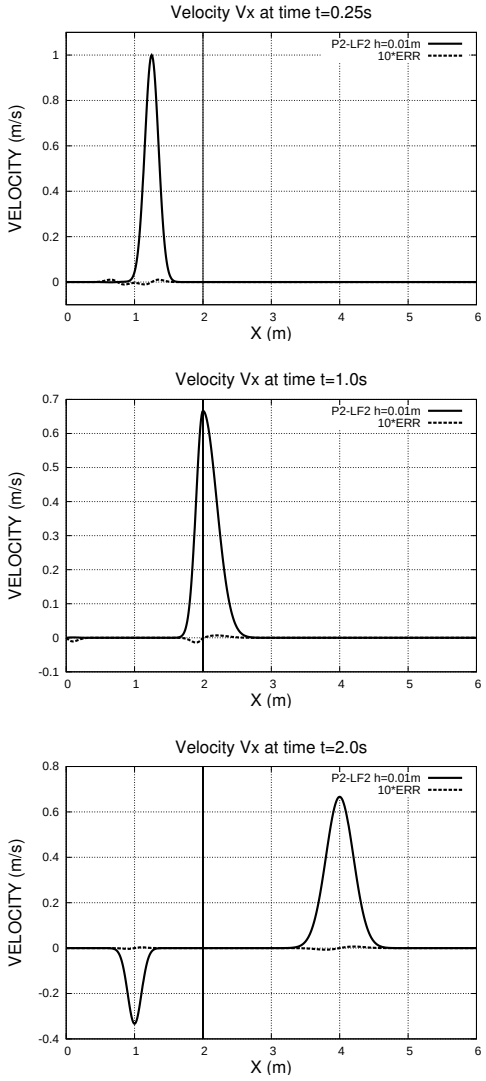

Figure 4: Propagation of a pulse in a heterogeneous medium containing medium1/medium2. Velocity v_x and error on the line $y = 0.5$ at times t_1=0.25s, t_2=1.0s and t_3=2.0s. Interface between media in x =2.

left boundary of the domain.

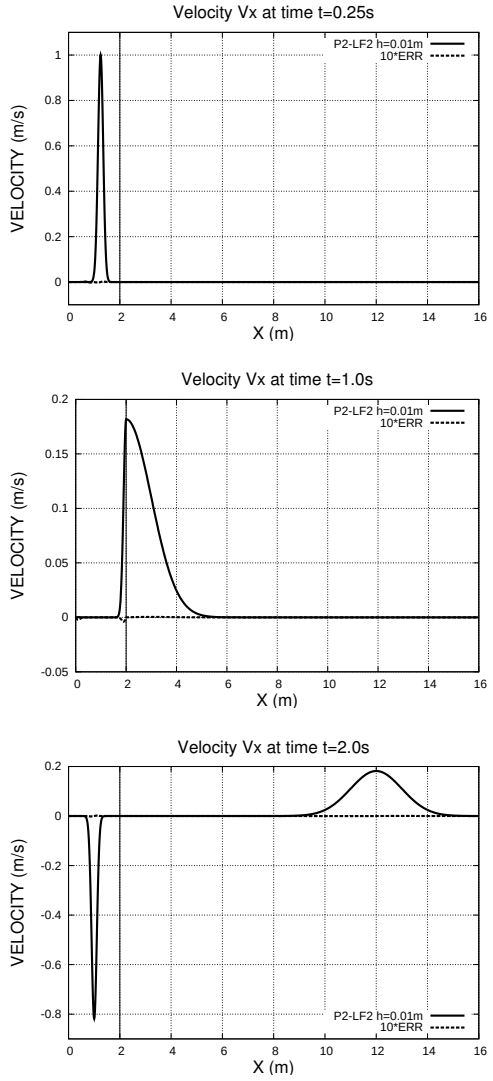

Figure 5: Propagation of a pulse in a heterogeneous medium containing medium1/medium3. Velocity v_x and error on the line $y = 0.5$ at times t_1=0.25s, t_2=1.0s and t_3=2.0s. Interface between media in x =2.

6 Explosive source in a homogeneous half space

Finaly, we study the Garvin test case [6] that is the propagation of waves generated by an explosive source in a homogeneous half-space as described in figure 6. We compare our solutions to a reference one resulting from a solver written by F.J. Sanchez-Sesma and L.E. Perez-Rocha [13]. The medium is homogeneous of density $\rho = 1$ kg/m^2 and P- and S-waves velocities of V_P =103.92 m/s and V_S=60 m/s respectively. We apply a free surface boundary condition on the upper boundary of the domain and absorbing conditions on the other boundaries.

Medium	1	1 | 2	1 | 3
Triangles	80 000	120 000	320 000
D.O.F	480 000	720 000	1 920 000
Δt (s)	$0.14\ 10^{-2}$	$0.70\ 10^{-3}$	$0.14\ 10^{-3}$
err_{L^2} at t_1	$0.21\ 10^{-2}$	$0.10\ 10^{-2}$	$0.21\ 10^{-3}$
err_{L^∞} at t_1	$0.21\ 10^{-2}$	$0.10\ 10^{-2}$	$0.22\ 10^{-3}$
CPU at t_1	36 s	135 s	1780 s
err_{L^2} at t_2	$0.18\ 10^{-2}$	$0.10\ 10^{-2}$	$0.46\ 10^{-3}$
err_{L^∞} at t_2	$0.21\ 10^{-2}$	$0.14\ 10^{-2}$	$0.39\ 10^{-3}$
CPU at t_2	146 s	462 s	6548 s
err_{L^2} at t_3	$0.14\ 10^{-2}$	$0.11\ 10^{-2}$	$0.62\ 10^{-3}$
err_{L^∞} at t_3	$0.19\ 10^{-2}$	$0.68\ 10^{-3}$	$0.17\ 10^{-3}$
CPU at t_3	294 s	918 s	12708 s

Table 4: Number of triangles, total number of degrees of freedom, time steps, errors in L^2 and L^∞ norm of v_x and CPU times for the propagation of a pulse in homogeneous and heterogeneous media

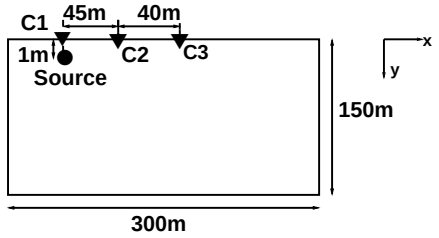

Figure 6: Explosive source in a half space. Source and sensors positions

The source is located at 1 m depth and three surface sensors are placed at the epicenter and at 45m and 95m from the first sensor respectively (figure 6). The source signal is a Ricker

$$s\left(t\right) = \left[-1. + 2\,a\left(t-0.3\right)^2\right]\ exp\left[-a\ \left(t-0.3\right)^2\right]$$

with $a = 159.42$. It has a central frequency about 4.0 Hz and a maximum frequency equal to 12.0 Hz. Thus, the wavelength Λ is approximately equal to 5.0 m. The explosive source is introduced as a right hand side on σ_{xx} and σ_{yy}. Initial conditions for the system are $\vec{V} = \vec{0}$ and $\vec{\sigma} = \vec{0}$ and solutions are calculated until $t = 2.5$ s. Our objective is to compare the results obtained with the P2-LF2 and P4-LF4 methods. To highlight the difference of both methods, we first use two uniform very coarse meshes : M1 with $h = 5.0$m and containing 3600 triangles and M2 with $h = 2.5$m and 14 400 triangles. We define an error (in %) between the solutions and the reference : for a given sensor and a component of the velocity, the error is the mean value of the relative errors calculated at the extrema of the profiles (between 3 and 6 values, as seen on fig. 7 to 9). We plot, in figures 7, 8 and 9, the profiles of v_y as a function of time obtained at the three sensors and for the two coarse meshes M1 and M2 (first and second lines of all figures). Note that, for a better visibility, the solutions ob-

tained at the three surface sensors have been plotted for different time windows.

Observing the different figures, it is obvious that the P4-LF4 method produces better solutions than the P2-LF2 method. For the coarsest mesh M1, the profiles of the P4-LF4 method contain all the characteristics of the reference solution. The results obtained with the mesh M2 are clearly closer to the reference solution but it still remains an important delay on the profile corresponding to the P2-LF2 method at sensor C1. Finally, we introduce a finer mesh, M3 for which h=1.0m and containing 90 000 triangles. We plot, in figures 7, 8 and 9 (last line), the solutions obtained with the P4-LF4 method. Except a slight delay of the solutions, especially at sensor C2, the results are satisfying and constitue a validation of our method.

The values of the mean relative errors on v_y, obtained for the different schemes and meshes are given in table 5. From the observation of the table, we notice that the errors on the amplitude of the solutions of the P4-LF4 method are lower than with the P2-LF2 method, at all sensors and with the three meshes since the values of the mean error are divided by 2. For the finest mesh M3, corresponding to a mesh spacing equal to $\Lambda/5$, the error level is satisfactory. We also remark that the convergence towards the reference solution is slower that expected, especially when compared to the results of the eigenmode problem. It is probably due to the absorbing condition which is a basic upwind scheme and would gain to be improved.

	P2-LF2	P4-LF4
C1 / M1	70	47
C1 / M2	60	10
C1 / M3	10	5
C2 / M1	50	12
C2 / M2	26	12
C2 / M3	10	4
C3 / M1	63	24
C3 / M2	33	12
C3 / M3	10	6

Table 5: Mean relative error (in %) on v_y at the three sensors

7 Conclusion

We proposed a fourth-order leap-frog time scheme combined with a high-order discontinuous Galerkin method for the solution of the elastodynamic equations. Following the previous results obtained in [3],[7] when global high-order accuracy is quested, it is worthless using higher-order space interpolation when keeping the classical leap-frog time scheme since accuracy is not improved while CPU costs are increased. This extension of the leap-frog scheme to fourth-order (or to any even order) modifies the classical leap-frog scheme in a multi-step procedure but where the additional cost is compensated by the use of greater time steps.

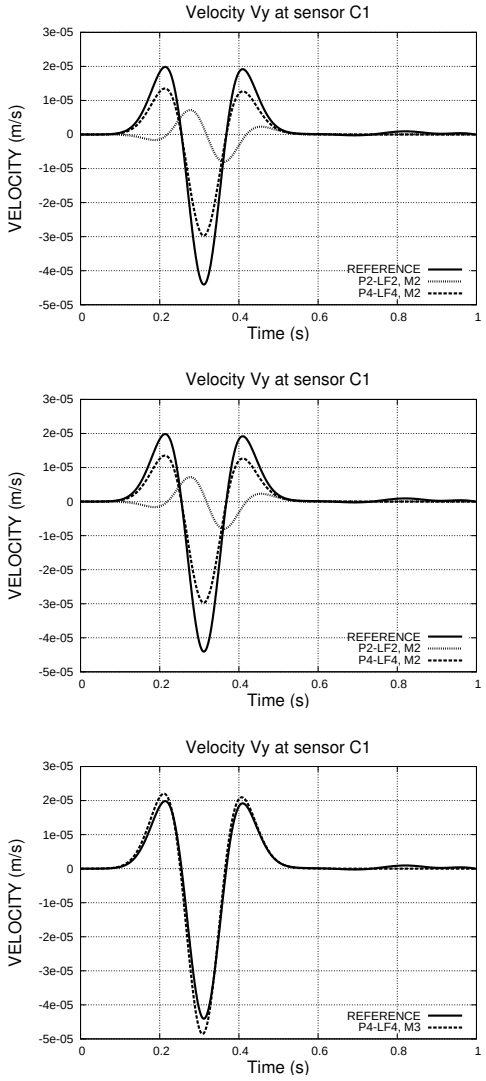

Figure 7: Profiles of v_y at the sensor C1 for the two coarse meshes M1 (first line) and M2 (second line) and the finest one (last line)

This method has been first applied to the propagation of an eigenmode which permits numerical studies of stability, convergence, accuracy and efficiency of the schemes. The propagation of a pulse in heterogeneous media proves the robustness of the method. The Garvin test case constitutes a validation of the source implementation. The first results, obtained in two space dimensions, are encouraging since a clear improvement of the results is obtained compared to methods based on second-order leap-frog scheme for a moderate increase in computational cost. Moreover, fourth-order convergence is reached with the P4-LF4 version when free surface conditions are considered. Implementation of this

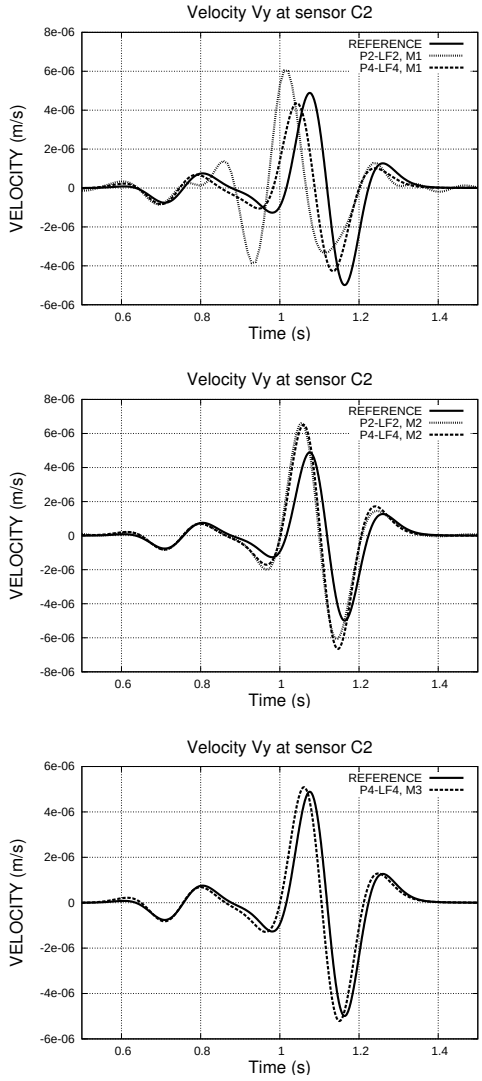

Figure 8: Profiles of v_y at the sensor C2 for the two coarse meshes M1 (first line) and M2 (second line) and the finest one (last line).

method in the three dimensional solver [3] is underway, accuracy and efficiency of methods being a key aspect towards realistic three dimensional simulations.

References

[1] M. Ben Jemaa, N. Glinsky-Olivier, V.M. Cruz-Atienza and J. Virieux, 3-D dynamic rupture simulations by a finite volume method, Geophys. J. Int., 178 (2009), 541-560.

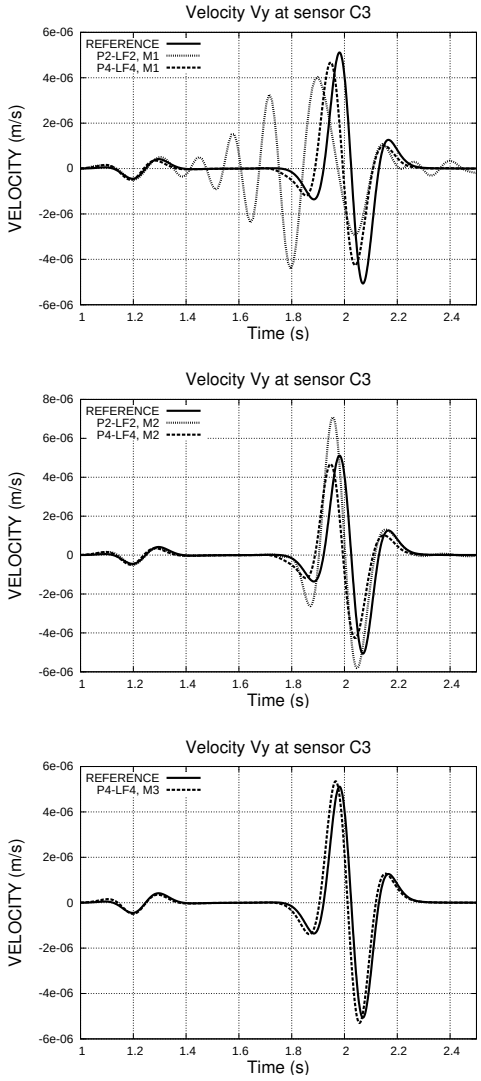

Figure 9: Profiles of v_y at the sensor C3 for the two coarse meshes M1 (first line) and M2 (second line) and the finest one (last line).

[2] P.G. Ciarlet, The Finite Element Method for Elliptic Problems, North-Holland, Amsterdam (1978).

[3] S. Delcourte, L. Fezoui and N. Glinsky-Olivier, A high-order discontinuous Galerkin method for the seismic wave propagation, ESAIM : Proceedings, 27 (2009), 70-89.

[4] H. Fahs, Méthode de type Galerkin discontinu d'ordre élevé pour la résolution numérique des équations de Maxwell instationnaires sur des maillages simplexes non-conformes, Thèse de doctorat de l'Université de Nice-Sophia Antipolis, décembre 2008.

[5] L. Fezoui, S. Lanteri, S. Lohrengel and S. Piperno, Convergence and stability of a Discontinuous Galerkin time-domain method for the 3D heterogeneous Maxwell equations on unstructured meshes, ESAIM: Math. Model. and Numer. Anal.,39,No.6 (2005), 1149-1176.

[6] W. W. Garvin, Exact transient solution of the buried line source problem, Proc. R. Soc. London Ser. A, 234 (1956), 528-541.

[7] M. Käser and M. Dumbser, An Arbitrary High Order Discontinuous Galerkin Method for Elastic Waves on Unstructured Meshes I: The Two-Dimensional Isotropic Case with External Source Terms, Geophys. J. Int. 166(2) (2006), 855-877.

[8] M. Käser, V. Hermann and J. de La Puente, Quantitative Accuracy Analysis of the Discontinuous Galerkin method for Seismic Wave Propagation, Geophys. J. Int., 173(3) (2008), 990-999.

[9] D. Komatitsch and J.-P. Vilotte, The spectral-element method: an efficient tool to simulate the seismic response of 2D and 3D geological structures, Bull. Seism. Soc. Am., 88 (1998), 368-392.

[10] P. Moczo, J. Kristek, V. Vavrycuk, R.J. Archuleta and L. Halada, 3D heterogeneous staggered-grid finite-difference modeling of seismic with volume harmonic and arithmetic averaging of elastic moduli and densities, Bull. Seism. Soc. Am. 92 (2002), 3042-3066.

[11] W. Reed and T. Hill, Triangular mesh method for neutron transport equation, Tech. Rep. LA-UR-73-479, Los Alamos Scientific Laboratory (1973).

[12] J.-F. Semblat and A. Pecker, Waves and vibrations in soils, IUSS Press, Pavia, Italy (2009).

[13] F.J. Sanchez-Sesma and U. Iturraran-Viveros, The Classic Garvin's Problem Revisited, Bull. Seism. Soc. Am. 96 (2006), 1344-1351.

[14] H. Spachmann, R. Schuhmann and T. Weiland, Higher Order Explicit Time Integration Scheme for Maxwell's Equations, Int. J. Numer. Model., 15 (2002), 419-437.

[15] J. Virieux, P-SV wave propagation in heterogeneous media: Velocity-stress finite difference method, Geophysics, 51 (1986), 889-901.

[16] Jeffrey L. Young, High order leapfrog methodology for the temporally dependent Maxwell's equations, Radio Science, 36 (2001), 9-17.

Centre de recherche INRIA Sophia Antipolis – Méditerranée
2004, route des Lucioles - BP 93 - 06902 Sophia Antipolis Cedex (France)

Centre de recherche INRIA Bordeaux – Sud Ouest : Domaine Universitaire - 351, cours de la Libération - 33405 Talence Cedex
Centre de recherche INRIA Grenoble – Rhône-Alpes : 655, avenue de l'Europe - 38334 Montbonnot Saint-Ismier
Centre de recherche INRIA Lille – Nord Europe : Parc Scientifique de la Haute Borne - 40, avenue Halley - 59650 Villeneuve d'Ascq
Centre de recherche INRIA Nancy – Grand Est : LORIA, Technopôle de Nancy-Brabois - Campus scientifique
615, rue du Jardin Botanique - BP 101 - 54602 Villers-lès-Nancy Cedex
Centre de recherche INRIA Paris – Rocquencourt : Domaine de Voluceau - Rocquencourt - BP 105 - 78153 Le Chesnay Cedex
Centre de recherche INRIA Rennes – Bretagne Atlantique : IRISA, Campus universitaire de Beaulieu - 35042 Rennes Cedex
Centre de recherche INRIA Saclay – Île-de-France : Parc Orsay Université - ZAC des Vignes : 4, rue Jacques Monod - 91893 Orsay Cedex

Éditeur
INRIA - Domaine de Voluceau - Rocquencourt, BP 105 - 78153 Le Chesnay Cedex (France)
http://www.inria.fr
ISSN 0249-6399